Full-field speckle interferometry for non-contact photoacoustic tomography

Jens Horstmann[1], Hendrik Spahr[2], Christian Buj[2], Michael Münter[2] and Ralf Brinkmann[1,2]

[1] Medical Laser Center Lübeck GmbH, Peter-Monnik-Weg 4, 23562 Lübeck, Germany
[2] Institute of Biomedical Optics, University of Lübeck, Peter-Monnik-Weg 4, 23562 Lübeck, Germany

E-mail: horstmann@mll.uni-luebeck.de

Abstract

A full-field speckle interferometry method for non-contact and prospectively high speed Photoacoustic Tomography is introduced and evaluated as proof of concept. Thermoelastic pressure induced changes of the objects topography are acquired in a repetitive mode without any physical contact to the object. In order to obtain high acquisition speed, the object surface is illuminated by laser pulses and imaged onto a high speed camera chip. In a repetitive triple pulse mode, surface displacements can be acquired with nanometre sensitivity and an adjustable sampling rate of e.g. 20 MHz with a total acquisition time far below one second using kHz repetition rate lasers. Due to recurring interferometric referencing, the method is insensitive to thermal drift of the object due to previous pulses or other motion. The size of the investigated area and the spatial and temporal resolution of the detection are scalable. In this study, the approach is validated by measuring a silicone phantom and a porcine skin phantom with embedded silicone absorbers. The reconstruction of the absorbers is presented in 2D and 3D. The sensitivity of the measurement with respect to the photoacoustic detection is discussed. Potentially, Photoacoustic Imaging can be brought a step closer towards non-anaesthetized *in vivo* imaging and new medical applications not allowing acoustic contact, such as neurosurgical monitoring or burnt skin investigation.

Keywords: photoacoustic tomography, non-contact detection of surface displacement, speckle interferometry, spatial phase shifting

(Some figures may appear in colour only in the online journal)

1. Introduction

Photoacoustic techniques for biomedical imaging have undergone rapid development over the last years; a recent review is given by Wang and Hu (2012). Photoacoustic Imaging is based on the emission of thermoelastic pressure waves after short-pulsed optical excitation of absorbers in a less absorbing environment. Thus, the pressure waves propagate through the tissue and can be detected at its surface. For tomographic imaging, the position of the absorbers can be reconstructed in 3D, using e.g. time reversal approaches or triangulation based algorithms like delay-and-sum (Hoelen and De Mul 2000, Treeby and Cox 2010).

The underlying contrast mechanism in Photoacoustic Imaging is optical absorption. Due to the diffuse propagation of the excitation light, deep seated absorbers can be reached. In medical applications, the high absorption contrast of different tissue chromophores enables e.g. imaging of dermal and subdermal blood vessels or tumour screening in mammography with a high intrinsic contrast, as shown by Heijblom *et al* (2011). The emitted pressure waves are subject to only low refraction and scattering.

Different methods have been employed to detect the thermoelastic signals. On the one hand, piezoelectric elements in contact with the surface are widely used. These transducers can be used as single elements in scanning mode for very high spatial resolution (Ku *et al* 2010) or parallelized in an array like in conventional ultrasound imaging (Buehler *et al* 2013). However, their use often limits the application versatility or shadows the excitation light, when applied from the same side.

As an alternative to piezoelectric detection, several optical techniques have been introduced. One approach is the laser beam interrogation of a Fabry–Perot film placed on the object, as shown by Laufer *et al* (2009). The film is modulating the reflected interrogation beam when affected by the pressure waves. Carp and Venugopalan (2007) suggested a two-wave-mixing interferometer for the non-contact detection of surface displacement, which however requires a thin water film on the surface. A completely non-contact method is proposed by Rousseau *et al* (2012), using a confocal Fabry–Perot interferometer in differential mode for the same purpose. These approaches require mechanical scanning of a single element detector over the object surface and consequently suffer from long acquisition times often in the range of several minutes, which is critical for *in vivo* imaging without the use of anaesthesia.

The aim of the project is to evaluate the potential of the full-field interferometric detection for non-contact Photoacoustic Tomography (PAT) with following targeted advantages: The method is potentially capable of acquiring a full photoacoustic dataset within a fraction of a second and works without any physical contact to the object. Furthermore, the method is versatile in terms of a scalable field of view and a scalable sampling rate, depending on the desired parameters. In combination, those attributes might be a step towards clinically usable devices.

2. Methods and material

2.1. Methods

For the realization of the non-contact PAT approach, a Mach–Zehnder based speckle interferometer (Buj *et al* 2014, Horstmann and Brinkmann 2014) is developed as photoacoustic detector as sketched in figure 1. The object surface is illuminated by a pulsed laser. The backscattered light is combined with a reference from the same source and imaged onto a high speed camera. Owing to the coherence of the illumination light, a speckle pattern is overlaid to the image. Due to the statistic formation, the phase of adjacent speckles is
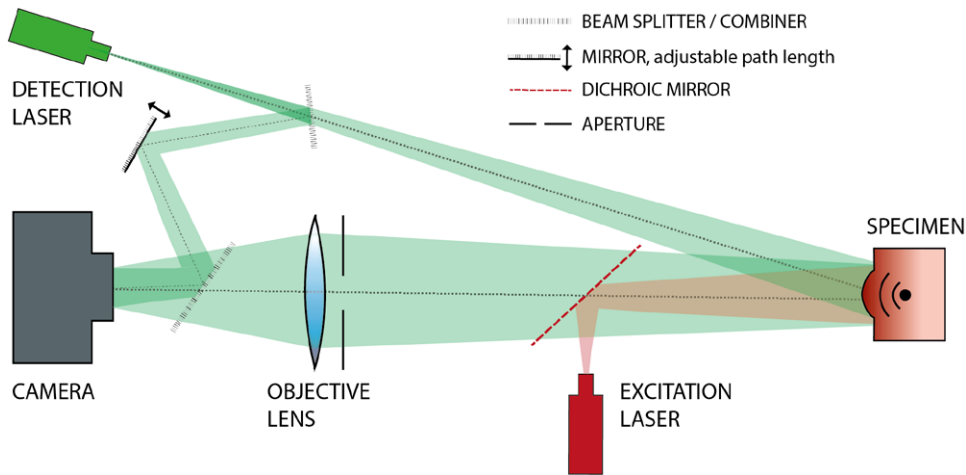
Figure 1. Interferometric detection of object surface displacement after photoacoustic excitation. The detection laser is illuminating a scalable surface area of e.g. $1\,cm^2$, which is imaged onto a digital camera sensor. If the topography is slightly altering after the pressure wave impact, the phase relation between object- and reference wave is influenced, which alters the captured interference pattern. The reference path length is adjustable to match with the object path within the coherence length.

unrelated, however, the phase within an individual speckle is constant (Jones and Wykes 1989). If the topography of the object changes slightly due to the pressure wave impact after photoacoustic excitation, the phase of the speckles is influenced due to the resulting phase difference between object- and reference wave. Phase shift or surface displacement, respectively, can be evaluated by spatial phase shifting electronic speckle pattern interferometry (sps ESPI, Pedrini *et al* 1993), which is explained in the following section. From the acquired displacement data, the position of the absorbers can be mathematically derived by the use of reconstruction algorithms.

2.1.1. Phase determination.　Since studies in this field (e.g. Payne *et al* 2003) have shown that the expected surface displacement induced by photoacoustic pressure is in the range $<100\,nm$, it is required to be capable of measuring with a sensitivity of a small fraction of the illumination wavelength. For this purpose, the object light field is overlaid with a reference. The resulting interferometric intensity on a discrete camera sensor with pixel columns $m = 1, ..., M$ and rows $n = 1, ..., N$ depends on the local intensities O and R of the object- and reference wave as well as on their local relative phase difference $\Phi_O - \Phi_R$:

$$I_{m,n} = O_{m,n} + R_{m,n} + 2\sqrt{O_{m,n} \cdot R_{m,n}}\ \cos(\Phi_{O_{m,n}} - \Phi_{R_{m,n}}). \tag{1}$$

For this study, ESPI in spatial phase shifting (sps) mode is implemented. Compared to the traditional temporal phase shifting (tps) mode, the calculation of the absolute object phase can be done from a single captured interferogram, as discussed by Knoche *et al* (2004). For the implementation of the sps mode, an additional phase gradient $\beta = (\beta_m, \beta_n)$ is introduced, which is overlaid to the speckle pattern:

$$\beta = (\beta_m, \beta_n) = \left(\frac{\Delta\Phi_R}{\Delta m}, \frac{\Delta\Phi_R}{\Delta n} \right), \tag{2}$$
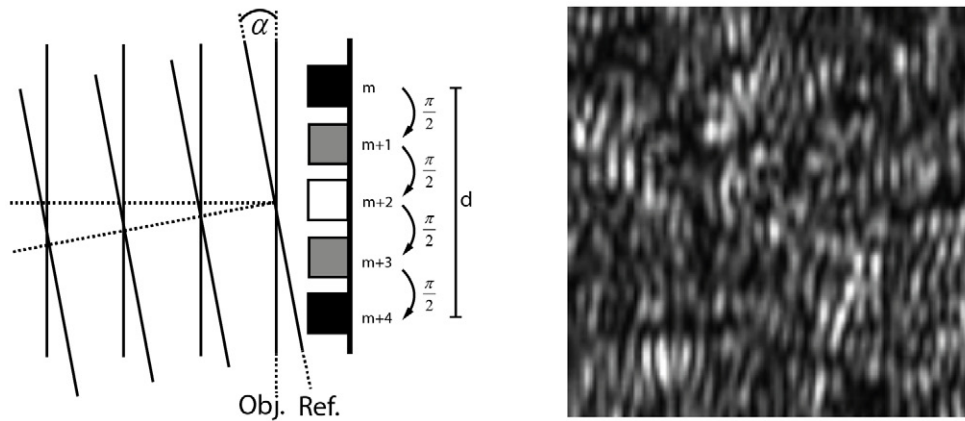
Figure 2. Left: the phase gradient is realized by an incidence angle between object and reference beam after their recombination. A variation of this angle varies the phase shift between adjacent pixels. Right: magnified section of the interference pattern. In this example, the phase gradient is realized horizontally. The resulting interference pattern consists of the speckled object surface image overlaid with the induced interferometric fringes.

where Φ_R represents the absolute reference phase. The interferometric intensity in each pixel can now be described as:

$$I_{m,n} = O_{m,n} + R_{m,n} + 2\sqrt{O_{m,n} \cdot R_{m,n}} \cos(\Phi_{O_{m,n}} - m\beta_m - n\beta_n + C). \tag{3}$$

The constant C describes a phase offset. The phase gradient can practically be implemented by combining the reference wave under an angle α (see figure 2, left). The wavelength λ and the magnitude of α determine the resulting fringe period d.

$$d = \frac{\lambda}{\sin(\alpha)}. \tag{4}$$

One fringe period corresponds to a phase shift of 2π and can be scaled to any number of adjacent pixels by varying α accordingly. The final interferogram consists of the speckled image surface and the fringes induced by the phase gradient (see figure 2, right).

The equation system (3) can be resolved for Φ_O in several different solutions (Knoche *et al* 2004), which differ mainly in the number of adjacent pixels taken into account. They also differ in performance for a particular situation in terms of the chosen magnitude of the phase gradient β_m. One possible solution is:

$$\Phi_{O_{m,n}} + m\beta_m = \text{atan2}\left[\left(\frac{1 - \cos\beta_m}{\sin\beta_m}\right)\frac{I_{m,n} - I_{m+2,n}}{2\,I_{m+1,n} - I_{m,n} - I_{m+2,n}}\right]. \tag{5}$$

By the use of algorithm (5), the absolute object phase can be derived from a single captured interferogram in case the boundary conditions for the sps ESPI method are satisfied: It is crucial that the minimum speckle size equals three pixels, because every speckle is sampled independently and the algorithm requires three adjacent pixels. Larger speckles are oversampled which is fine for the phase calculation but lowers the imaging resolution; a lower speckle size results in undersampling and consequently wrong results. Practically, the medium speckle size can be influenced by an imaging aperture.

Finally, acquiring Φ_O can be used to calculate the photoacoustic displacement if sampled over time, as explained in the following section.

2.1.2. Displacement determination. For the determination of surface displacement by the measurement of the absolute object phase, at least two phase images need to be acquired in order to take their difference $\Delta\Phi_{m,n}$ between the times t_1 and t_2. For an interferometric setup, the measured phase difference can be converted into the underlying geometrical displacement $\Delta S_{m,n}$:

$$\Delta S_{m,n} = \Delta\Phi_{m,n} \cdot \frac{\lambda}{4\pi} \cdot \gamma, \text{ with}$$
$$\Delta\Phi_{m,n} = \Phi_{O,t_2,m,n} - \Phi_{O,t_1,m,n},$$

(6)

where γ is a geometrical factor which depends on the incidence- and detection angle regarding the measured surface and equals 1 for an angle of incidence and detection perpendicular to the surface.

A reconstructable photoacoustic dataset consists of a stack of phase difference images. Each phase difference image corresponds to a particular time delay between the excitation pulse and the corresponding illumination pulse, so the transient photoacoustic signal can be sampled in its different states by repetitive measurements and increasing the delay in steps of Δt. In order to obtain the pure photoacoustic induced surface displacement under exclusion of the slower thermal drift of the volume due to previous excitation pulses and other object movements, the reference phase measurement Φ_{O,t_1} is taken before each excitation pulse and the photoacoustic measurement Φ_{O,t_2}. The method is therefore performed in a repetitive triple pulse mode, as shown in figure 3.

Prior to and after each excitation pulse, the interferogram is recorded in separate camera frames. The time delay between excitation pulse and second illumination pulse is slightly increased in steps of Δt with every repetition. The choice of the delay step size determines the temporal resolution of the resulting photoacoustic dataset. As an example, 100 ns delay steps refer to a resulting sampling rate of 10 MHz. The maximum delay in the last repetition of the measurement determines the highest detection depth.

2.1.3. Pre-processing. The displacement images are laterally smoothed by a Gaussian filter of 12 pixels in size applied in the spectral domain in order to minimize speckle artefacts. Due to temporal jittering of the illumination laser in the range of $\pm 0.5\,\mu$s, the displacement measurement is not equidistant in time and not in the right order. To overcome this hardware limitation, illumination- and excitation pulses are monitored by photodiodes and the corresponding time delay is attached to the displacement images as a time stamp. The stack of displacement images is sorted by the exact time delays after the measurement. The data are temporally spline-interpolated to an equidistant time grid after the data acquisition is completed. The noise level for a specific measurement is determined and signals are set to zero when weaker than the noise level.

2.1.4. Reconstruction method. In order to reconstruct the location of the photoacoustic sources, a 3D delay-and-sum beamforming algorithm, as formerly presented by Hoelen and De Mul (2000), has been implemented. Delay-and-sum approaches are based on the time of arrival of an acoustic signal from a specific volume element (voxel) to a specific measurement location and the speed of sound of the volume.
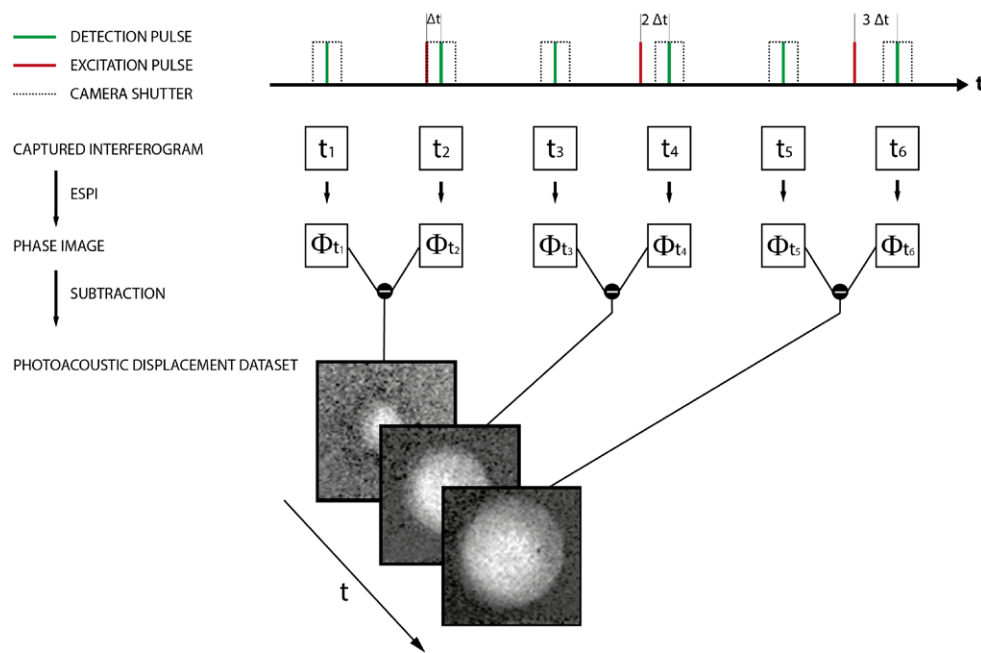
Figure 3. Triple pulse detection principle. In each camera frame with an odd index, an interferogram related to the undisturbed surface is recorded. In each frame with an even index, an interferogram related to the displaced surface is captured with an increasing time delay of multiple Δt after the excitation pulse. This procedure is carried out until the desired maximum time delay corresponding to a certain imaging depth is reached. From each interferogram, the absolute object phase is extracted by the use of the sps ESPI algorithm (equation (5)). The phase images of each pair of reference and deformation captures are subtracted. The result is a time-dependent displacement dataset.

The volume to be reconstructed is divided into $X \cdot Y \cdot Z$ discrete voxels with the edge length l, that are denoted by their integer indices (x, y, z). One voxel is the smallest reconstructable source. The original $M \cdot N$ detector matrix (m, n) is laterally spline-interpolated to a detector matrix (m^*, n^*) of the size $X \cdot Y$ to fit the element size of the voxels of the reconstruction matrix. Now, each detector element is located on the upper surface of an upper layer voxel (figure 4).

For each voxel (x, y, z), the distance r from its centre to a surface element (m^*, n^*) is defined by

$$\overrightarrow{|r|} = l\sqrt{(x - m^*)^2 + (y - n^*)^2 + (z - 1/2)^2}. \tag{7}$$

The propagation time τ for an acoustic signal originating from a voxel (x, y, z) to reach a surface element (m^*, n^*) at the speed of sound c is therefore given by

$$\tau = \frac{\overrightarrow{|r|}}{c}. \tag{8}$$

The times from a source within each voxel to reach each surface element are calculated and written in a propagation matrix. The delay-and-sum algorithm picks those parts of the time line of each detector element, which are corresponding to the specific propagation time from
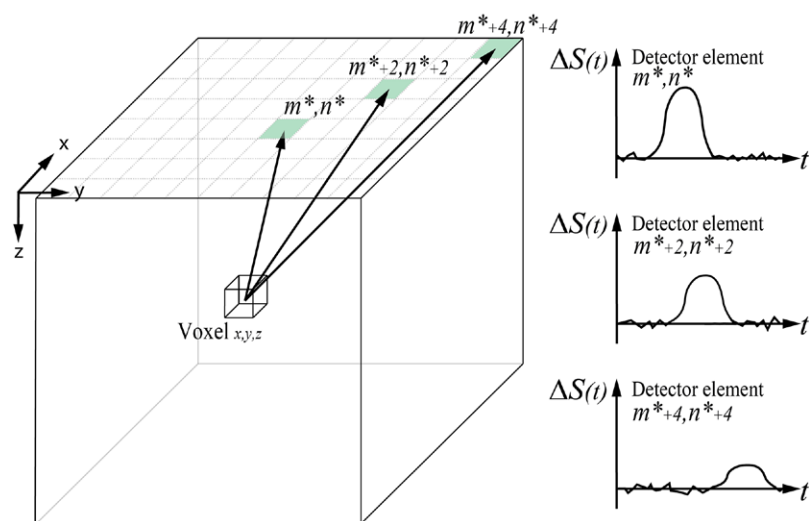
Figure 4. The volume to be reconstructed is divided into voxels. The magnitude of the vectors are determining the expected time of arrival of a propagating signal from the voxel under consideration.

the voxel under consideration. The photoacoustic source intensity A for the voxel can finally be obtained by the summation of the corresponding times of all detector elements.

$$A(x, y, z) = \sum_{m*=1, \, n*=1}^{X,Y} \Delta S_{m*,n*}(\tau_{m*,n*}(x, y, z)). \qquad (9)$$

2.1.5. Quality dependent weighting. During the reconstruction, a signal-quality dependent weighting is applied. With regard to the previous section, one voxel is the smallest reconstructable source. Our weighting method examines the consistency of the detected signals in their temporal and spatial development under the assumption that the photoacoustic signal of a single voxel is expected as a spherical wave over time. By this means, signals are processed weighted or thresholded, respectively, if the consistency is exceeding a certain value q. This procedure makes a thresholding of the finally reconstructed image unnecessary. Strictly assigning a location as a function of the time of arrival leads to arcing artefacts as described by Carp and Venugopalan (2007). The used method is beneficial for objects with relatively few sources or sparse signal matrices, respectively.

2.2. Material

As a light source for the interferometer, a Q-switched, frequency doubled Nd:YAG laser (CryLas FTSS 355-50, wavelength 532 nm, repetition rate 20 Hz, pulse duration 1 ns, pulse energy 100 µJ, 15 mm expanded beam diameter) was used. A digital camera (Basler Pilot piA1600-35g, resolution 1600×1200 pixels, pixel size 7.4 µm) was used with a frame rate of 20 Hz to capture the interferograms. Photoacoustic excitation was performed using a Nd:YAG laser (Quantel YG571C, wavelength 1064 nm, repetition rate 10 Hz, pulse duration 6 ns). The choice for this wavelength was mainly because of the high penetration depth of infrared light. For the planned medical applications, the wavelength will be shifted to a range where the

absorption and the absorption contrast for the target chromophore is high. The radiant exposure on the specimen was between 15 and 32 mJ cm^{-2}. By the use of the repetitive triple pulse approach described in 2.1.2, the photoacoustic data acquisition can be performed with a scalable sampling rate of e.g. 10 MHz, although the components are rather slow.

The lateral resolution of the displacement measurement or imaging resolution, respectively, is influenced by optical and ESPI parameters like the medium speckle size (set to 4 pixels), the sps phase period on the chip (set to 4 pixels), the pixel pitch of the detector array (7.4 μm) and the imaging scale (set to 1). Furthermore, a Gaussian blur filter with 12 pixels in size was applied to the complex phase maps in order to reduce speckle artefacts. These parameters in combination lead to a resolution of 90 μm in the presented measurements.

As a specimen for the first presented measurement, a transparent silicone cube (Wacker Silicones RT604 A/B) with an embedded black silicone spherical absorber with 1 mm in diameter was built (see figure 5, left). The detection surface was coated with a 150 μm thick layer of white silicone to increase backscattering of the detection laser light. The absorption coefficient of the black silicone was measured to be 29.6 cm^{-1} for the used excitation wavelength. The acoustic properties of the phantom material were measured to be 0.96 mm μs^{-1} for the speed of sound. The thermal expansion coefficient is 3×10^{-4} m K^{-1}.

For the tissue phantom, two 4×6 cm^2 pieces of the epidermis of porcine ears were isolated from the central back side of the ear after the hair was removed with the help of depilatory cream. The layers were about 2 mm thick. The inner sides of the skin faced each other with a cubic 1 mm black silicone absorber and some ultrasound gel in between (see figure 5, right). The detection side was coated with a thin layer of white latex in order to increase backscattering.

3. Results

3.1. Silicone phantom measurements

100 displacement maps were acquired from 200 captured interferograms using the ESPI phase determination algorithm (equations (5) and (6)). By varying the time delay between excitation and detection, the acquisition is covering the time interval from excitation to 10 μs after excitation. The applied radiant exposure was 32 mJ cm^{-2} on a spot of 5 mm in diameter. For ease of operation, the detection was performed on an orthogonal side of the phantom. The illumination was performed at an angle of 45°, the detection at 0° (camera sensor parallel to the object surface), the resulting geometrical factor γ was 0.86 (see equation (6)).

Some representative phase difference images are presented in figure 6, in which the left column shows the ESPI raw data with the recorded phase differences converted to axial displacements with respect to equation (6). The right column shows the filtered data, as described in 2.1.3.

The time series shows the development of the phase shift or surface displacement, respectively. Displayed times are relative to the excitation pulse. After the propagation delay of about 3.5 μs, a spherical deformation as an interaction of the spherical pressure wave with the free boundary is observed, which is visible in the outer regions with proceeding time.

The image reconstruction of the silicone phantom is shown in figure 7. The reconstruction is performed from the pre-processed data (see section 2.1.3). Cross sections are shown left and in the middle. In the left part, typical arcing artefacts appear, which are eliminated by the use of the quality dependent weighting as described in section 2.1.5. The consistency factor q was set to 0.8 in the presented image reconstructions, which means that signals were considered in the reconstruction if the spherical wave originating from each voxel was complete at least
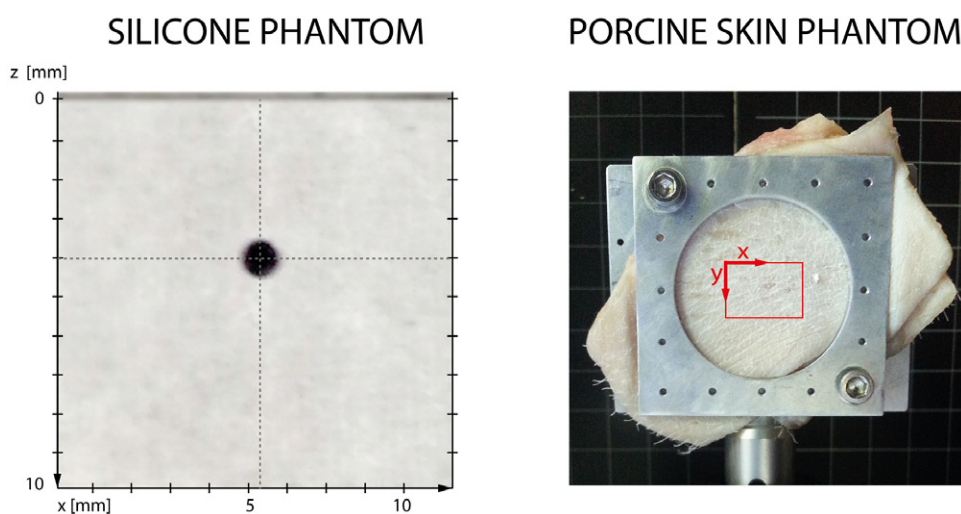
Figure 5. Left: photography of the *x*–*z* plane of the silicone phantom, the darker layer on top is the white silicone layer on the detection side. Right: tissue phantom in the phantom holder. The investigated area is marked red.

80%. The right part shows the weighted volumetric reconstruction. No subsequent thresholding was applied.

3.2. Porcine skin measurements

In this measurement, 300 phase difference images were acquired within $3\,\mu$s after excitation. For ease of operation, photoacoustic excitation was performed from the back side of the phantom under a small angle. The radiant exposure was $15\,$mJ$\,$cm^{-2} on an area of $1.5\,$cm^2. The image reconstruction is shown in figure 8.

4. Discussion

A novel full-field speckle-based interferometric detection method for non-contact PAT has been realized and first measurements to demonstrate the practical feasibility were undertaken. Embedded black silicone objects served as absorbers in a silicone matrix and in a porcine skin phantom. The study demonstrated that photoacoustic surface displacements can be acquired by the use of speckle interferometry in a repetitive pulsed mode. The measured photoacoustic axial displacement was in the range of $50\,$nm. The sensitivity of the displacement measurement is around $1\,$nm, the imaging resolution is $90\,\mu$m. The effective photoacoustic temporal sampling rate was $10\,$MHz in the presented measurements and is scalable to higher or lower values by varying the delay steps in the repetitive measurement. The acquired photoacoustic data is suitable for reconstruction. Using excitation radiant exposures of $15\,$mJ$\,$cm^{-2} which is within the corresponding safety limit of the American National Standards Institute ($20\,$mJ$\,$cm^{-2}) in the porcine skin phantom, the signal to noise ratio (SNR) of the displacement measurement was sufficient for reconstruction. For the silicone phantom, the excitation radiant exposure was chosen higher ($32\,$mJ$\,$cm^{-2}) in order to get a higher SNR for this proof of concept measurement which resulted in an excellent reconstruction.
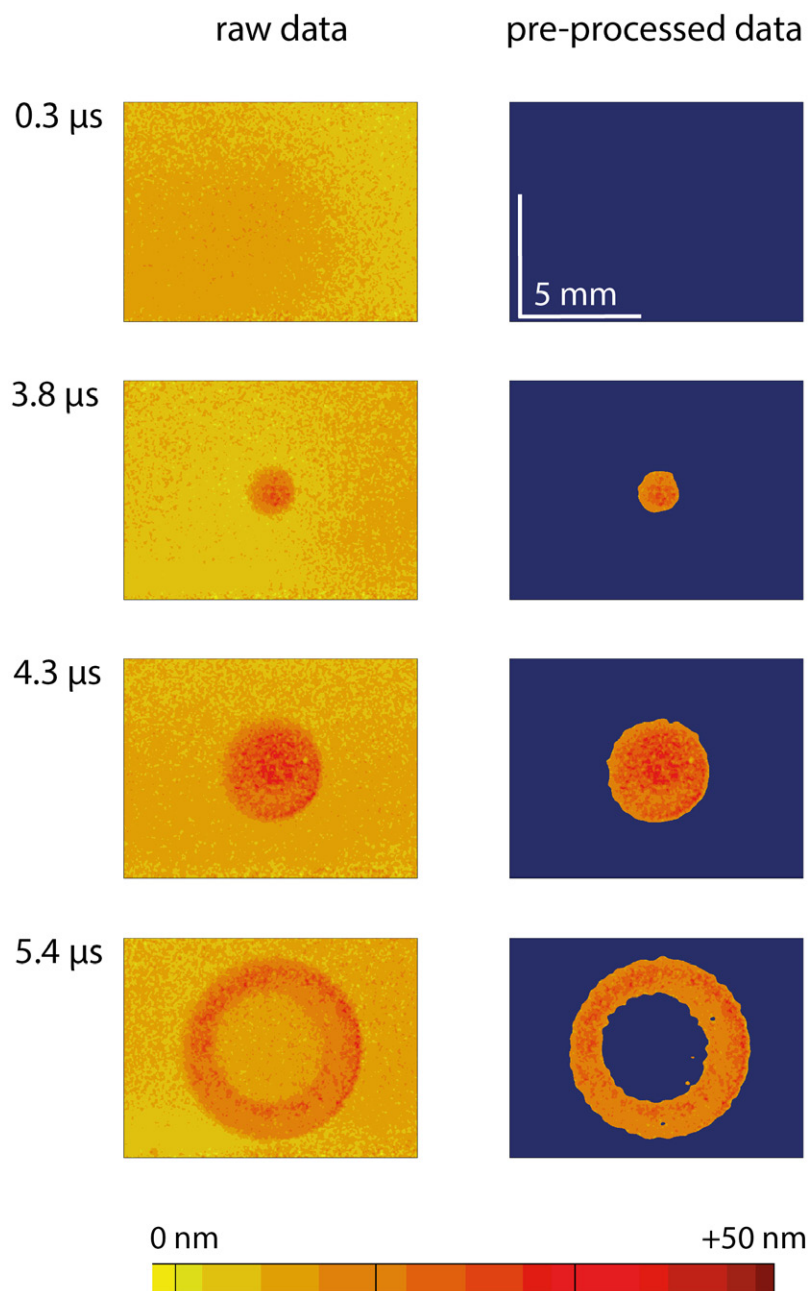
raw data   pre-processed data

Figure 6. Representative surface displacement images. Left: raw data. Right: segmented and thresholded data. The maximum measured displacement is about 50 nm in this measurement.

By the use of a quality dependent weighting of the acquired signals, the reconstructions showed no streak artefacts and no subsequent thresholding was necessary. The displacement data of the silicone phantom had a high SNR of about 50 and the reconstruction of the embedded spherical absorber is accurate in size and position. In the porcine skin measurement, the
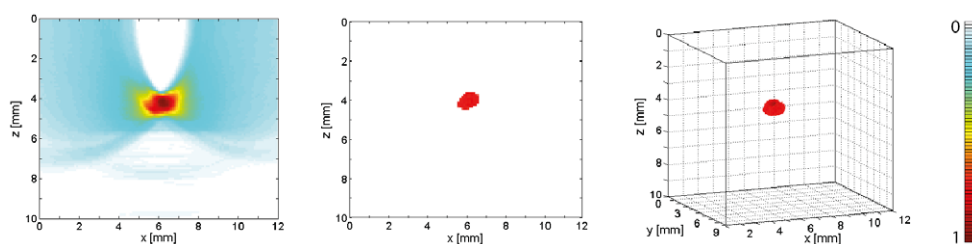
Figure 7. Cross section of the volumetric image reconstruction without (left) and with weighting (middle). Right: weighted reconstructed volume. The reconstruction intensity is normalized (see colour bar).
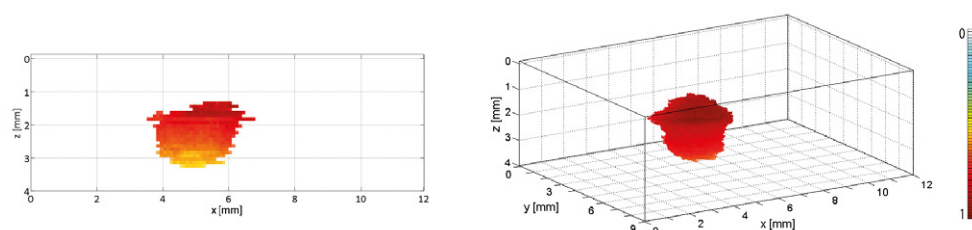

Figure 8. Left: *x/z* section of the reconstruction of the porcine skin phantom, right: reconstructed volume.

silicone cube which was embedded between two 2 mm thick porcine skin pieces could be reconstructed correctly in position. However, this reconstruction showed more artefacts and an inaccurate morphology of the embedded absorber. This is attributed to higher noise due to the more complex and inhomogeneous phantom structure. The acoustic velocity mismatch between the embedded silicone absorber and the surrounding porcine skin tissue was not considered in the reconstruction. Furthermore, the irregular pulse to pulse jitter of the detection laser of up to $\pm 0.5\,\mu$s made a temporal interpolation of the displacement signals necessary, which caused notable errors. The implementation of an actively Q-switched laser with a low temporal jitter will make the temporal interpolation unnecessary and consequently eliminate interpolation errors, which apparently lower the reconstruction quality.

Prospectively, the acquisition speed can be significantly improved compared to the proof of concept measurements presented in this paper. A short acquisition time is an important criterion for the practical clinical usability. In order to achieve e.g. 10 MHz sampling rate and a detection depth of 15 mm in tissue, 100 ns delay steps over a total acquisition window of $10\,\mu$s are required. Therefore, 100 displacement maps need to be recorded, which can be calculated from 200 captured interferograms. Accordingly, a full data set for volumetric reconstruction can be acquired in 100 ms, if an excitation rate of 1 kHz and a twice as fast detection rate is used. Therefore, a 2 kHz camera and an appropriate kHz laser systems can be used, which are commercially available for reasonable costs.

In the presented measurements, the excitation was performed from the orthogonal side or the backside of the phantoms. With respect to medical applications, excitation and detection from the same side is preferable. There are several possibilities to forego the surface coating used in the presented measurements as described in 2.2, e.g. by the use of a polarization sensitive detection which is suppressing the majority of photons that are backscattered in the depth of the specimen.

The photoacoustic signal amplitude is finally limited by safety guidelines regarding the maximum radiant exposure when imaging *in vivo* tissue. The sensitivity or SNR, respectively, is a crucial point in the use of the proposed method for PAT and is therefore discussed in detail.

4.1. Displacement determination sensitivity

ESPI is detecting phase differences by subtracting subsequently acquired phase images. The phase images are calculated by the ESPI algorithm, which is taking into account the intensities of adjacent pixels (equations (5) and (6)). The phase measurement is influenced by the underlying noise level. By the use of a stable laser source and a passively cooled laser and camera in the setup on an isolated optical table, the noise can be minimized to the shot noise level, depending on the amount of available light and the capacity of the camera pixels. The full well capacity (*fwc*) of the used model is below 20.000 e^-, so the shot noise number of electrons is $\sqrt{fwc} = 141\ e^-$ or at least 0.7% of the dynamic range, respectively. For an 8 bit (256 counts) capture of an interferogram, this means a statistical fluctuation of 1.8 bit. Due to error propagation, a variation of the pixel intensities (as input for equation (5)) can lead to deviation in the displacement measurement result (equation (6)) in the range of ± 1 nm.

The comparison of the photoacoustic signal amplitude and the noise floor describes the SNR of the displacement measurement. For an e.g. 1 mm silicone absorber in the depth of 4 mm and excitation energies within the corresponding safety limit, the geometrical out of plane deformation was around 50 nm in the presented measurements. Assuming the shot noise limit of ± 1 nm, the resulting SNR is about 50.

4.2. Photoacoustic sensitivity

In non-contact optical detection of photoacoustic signals, the measured variable is the surface displacement, while in the more common use of piezoelectric transducers, the acoustic pressure is measured. The pressure on the surface is proportional to the temporal derivative of the surface displacement, as discussed e.g. by Speirs and Bishop (2013). It is noted that the photoacoustic surface displacement is purely positive, while photoacoustic pressure is a transient bipolar signal and has a positive and negative part.

The pressure p within the tissue and the resulting displacement ξ in the direction to the wavefront normal at the free tissue boundary are connected by the acoustic impedance Z of the tissue:

$$p = \frac{Z}{2}\frac{\partial \xi}{\partial t}. \tag{10}$$

The factor of two describes that the particle displacement at the free boundary is twice the particle displacement within the tissue (Rousseau *et al* 2012).

This connection can be used to estimate the noise equivalent pressure of the photoacoustic detection approach: By taking $\partial \xi/\partial t$ of a 1 MHz displacement function and taking 1.5×10^6 Pa s m^{-1} as the acoustic impedance for soft tissues, the noise equivalent displacement is 1.5 kPa. With respect to the noise discussion in section 4.1, this value can be improved by the implementation of a detector array with a higher full well capacity. The price for the parallelized optical detection of photoacoustic surface displacement is a loss of sensitivity in contrast to the use of a point detector with a significantly higher full well capacity, however with the need for sequential raster scan detection.

5. Conclusion

In conclusion, the presented data show the high potential of the proposed full-field speckle interferometry approach for PAT which is a step towards clinical Photoacoustic Imaging, especially in cases when acoustic contact is unfavourable. With respect to the high imaging speeds, *in vivo* data acquisition without fixation of the subject and without the use of anaesthesia is feasible. Considering the presented results, it seems realistic to image chromophore structures in the range of 1 mm in diameter in a depth of up to 10 mm. The detection works in non-contact and prospectively with a high speed acquisition. The approach seems highly practical and versatile when employed in the reflection mode by means of excitation and detection performed from the same side. The area of the investigated field is scalable by optical magnification. The temporal sampling rate and the resulting acquisition time of the photoacoustic measurement can be scaled to the desired parameters.

The targeted imaging parameters seem generally appropriate for a clinically usable photoacoustic system for diagnosis (e.g. melanoma detection, mammography, gastroenterological investigation via endoscope) or monitoring purposes (neurosurgical interventions, burnt skin treatment, anaesthesia depth monitoring). Furthermore, the non-contact mode can open up new medical application fields, in cases when acoustic contact is impossible like in brain surgery or intraluminal interventions, where the system can be adapted to an operational microscope or an endoscope, respectively.

Next steps in the project are the implementation of high speed components, which work at repetition rates of 2 kHz, enabling the acquisition of a full 10 MHz photoacoustic dataset within the fraction of a second. The error-prone temporal interpolation of the signals will be unnecessary due to the use of lower jittering lasers, which will significantly improve the reconstruction quality.

Acknowledgments

References

Buehler A, Kacprowicz M, Taruttis A and Ntziachristos V 2013 Real-time handheld multispectral optoacoustic imaging *Opt. Lett.* **38** 1404–6
Buj C, Horstmann J, Münter M and Brinkmann R 2014 Speckle-based holographic detection for non-contact photoacoustic tomography *Proc. Biomed. Tech.* **59** 844–7
Carp S and Venugopalan V 2007 Optoacoustic imaging based on the interferometric measurement of surface displacement *J. Biomed. Opt.* **12** 0640011
Heijblom M, Klaase J M, van den Engh F M, van Leeuwen T G, Steenbergen W and Manohar S 2011 Imaging tumor vascularization for detection and diagnosis of breast cancer *Technol. Cancer Res. Treat.* **10** 607–23
Hoelen C G and De Mul F F 2000 Image reconstruction for photoacoustic scanning of tissue structures *Appl. Opt.* **39** 5872–83
Horstmann J and Brinkmann R 2014 Optical full-field holographic detection system for non-contact photoacoustic tomography *Proc. SPIE* **8800** 7
Jones R and Wykes C 1989 *Holographic and Speckle Interferometry (Cambridge Studies in Modern Optics)* vol 6 (Cambridge: Cambridge University Press) doi:10.1002/zamm.19850650203

Knoche S, Kemper B, Wernicke G and von Bally G 2004 Modulation analysis in spatial phase shifting electronic speckle pattern interferometry and application for automated data selection on biological specimens *Opt. Commun.* **270** 68–78

Ku G, Maslov K, Li L and Wang L V 2010 Photoacoustic microscopy with 2-μm transverse resolution *J. Biomed. Opt.* **15** 02130201

Laufer J, Zhang E, Raivich G and Beard P 2009 3D noninvasive imaging of the vasculature in the mouse brain using a high resolution photoacoustic scanner *Appl. Opt.* **48** D299–306

Payne B P, Venugopalan V, Mikic B B and Nishioka N S 2003 Optoacoustic tomography using time-resolved interferometric detection of surface displacement *J. Biomed. Opt.* **8** 273–80

Pedrini G, Pfister B and Tiziani H 1993 Double pulse-electronic speckle pattern interferometry *J. Mod. Opt.* **40** 89–96

Rousseau G, Bloulin A and Monchalin J-P 2012 Non-contact photoacoustic tomography and ultrasonography for tissue imaging *Biomed. Opt. Express* **3** 16–25

Speirs R W and Bishop A I 2013 Photoacoustic tomography using a Michelson interferometer with quadrature phase detection *Appl. Phys. Lett.* **103** 0535011

Treeby B and Cox B 2010 K-wave: MATLAB toolbox for the simulation and reconstruction of photoacoustic wave fields *J. Biomed. Opt.* **15** 02131401

Wang L V and Hu S 2012 Photoacoustic tomography: *in vivo* imaging from organelles to organs *Science* **335** 1458–62